

Alma Mater Studiorum Università di Bologna  
Archivio istituzionale della ricerca

Compressive sensing of full wavefield data for Structural Health Monitoring applications

This is the final peer-reviewed author's accepted manuscript (postprint) of the following publication:

*Published Version:*

Compressive sensing of full wavefield data for Structural Health Monitoring applications / Di Ianni, T.; De Marchi, L.; Perelli, A.; Marzani, A.. - In: IEEE TRANSACTIONS ON ULTRASONICS FERROELECTRICS AND FREQUENCY CONTROL. - ISSN 0885-3010. - STAMPA. - 62:7(2015), pp. 7152731.1373-7152731.1383. [10.1109/TUFFC.2014.006925]

*Availability:*

This version is available at: <https://hdl.handle.net/11585/475773> since: 2015-12-04

*Published:*

DOI: <http://doi.org/10.1109/TUFFC.2014.006925>

*Terms of use:*

Some rights reserved. The terms and conditions for the reuse of this version of the manuscript are specified in the publishing policy. For all terms of use and more information see the publisher's website.

This item was downloaded from IRIS Università di Bologna (<https://cris.unibo.it/>).  
When citing, please refer to the published version.

(Article begins on next page)

This is the final peer-reviewed accepted manuscript of:

*T. Di Ianni, L. De Marchi, A. Perelli and A. Marzani, "Compressive sensing of full wave field data for structural health monitoring applications" in IEEE Transactions on Ultrasonics, Ferroelectrics, and Frequency Control, vol. 62, no. 7, pp. 1373-1383, July 2015*

The final published version is available online at:

<https://doi.org/10.1109/TUFFC.2014.006925>

Rights / License:

The terms and conditions for the reuse of this version of the manuscript are specified in the publishing policy. For all terms of use and more information see the publisher's website.

*This item was downloaded from IRIS Università di Bologna (<https://cris.unibo.it/>)*

***When citing, please refer to the published version.***

# Compressive Sensing of Full Wavefield Data for Structural Health Monitoring Applications

Tommaso Di Ianni, Luca De Marchi, *Member, IEEE*, Alessandro Perelli,  
and Alessandro Marzani

## Abstract

Numerous non destructive evaluations and structural health monitoring approaches based on guide waves rely on analysis of wavefields recorded through scanning laser Doppler vibrometers (SLDVs) or ultrasonic scanners. The informative content which can be extracted from these inspections is relevant. However, the acquisition process is generally time-consuming posing a limit in the applicability of such approaches. In order to reduce the acquisition time, in this work a random sampling scheme based on Compressive Sensing (CS) is used to minimize the number of points in which the field is measured. The CS reconstruction performance is mostly influenced by the choice of a proper decomposition basis to exploit the sparsity of the acquired signal. Here, different basis have been tested to recover the guided waves wavefield acquired on both an aluminum and a composite plate. Experimental results show that the proposed approach allows to reduce the measurement locations required for accurate signal recovery to less than 34% of the original sampling grid.

## Keywords

Lamb waves, Compressive sensing, Defect detection, NDE, Full wavefield imaging.

1

## I. INTRODUCTION

2 During last decades, the constant need to improve the operational safety of structures is driving  
3 the development of nondestructive evaluation methods and monitoring systems aimed at the ongoing  
4 assessment of the health conditions of the structures. Structural health monitoring (SHM) includes  
5 a wide range of diagnostic techniques that allow the real-time evaluation of both the existence and  
6 entity of defects, reducing life-maintenance costs of structural components. For what concern plate-like  
7 components, diagnostic methods bases on guided wave [1], [2] have emerged as a viable option among  
8 ultrasonic methods because of the ability of such waves to travel long distances with reduced energy loss.

9 In particular, the visualization of the guided waves full wavefield propagating into the structure can show  
10 the waves interaction with structural features, turning out to be a suitable tool to automatically detect the  
11 presence of flaws [3].

12 A common way to obtain wavefield data consists of exciting the structure using a piezoelectric PZT  
13 transducer while acquiring guided wave responses at the user-defined spatial and temporal resolution  
14 by means of a scanning laser Doppler vibrometer [4], [5]. Such vibrometer measures the out-of-plane  
15 surface velocity in a grid of equispaced points over the structure. In such application, to reduce the effect  
16 of acquisition noise, multiple time traces are acquired at every scan point, making such a process rather  
17 time consuming.

18 However, if the wavefield signal can be sparsely decomposed in a limited number of basis functions a  
19 novel sensing paradigm can be applied. Such paradigm is based on the Compressive Sensing theory [6]  
20 which asserts that, thanks to sparsity, a signal can be acquired and recovered from a limited number (much  
21 smaller than what Shannon/Nyquist theorem suggests) of linear measurements without loss of information.  
22 CS methods have been used for ultrasonic data reduction [7], [8], [9], [10], and in exploration seismology  
23 [11] [12] to speed up the data acquisition phase. In these latter papers, it has been shown that a very  
24 good reconstruction of the wavefield can be achieved by using a random sampling procedure with some  
25 constraints enforced to limit the maximum sample distance, i.e. spatial gap.

26 In the contest of guided wave inspections, CS has been used as a powerful mean to perform signal  
27 decomposition and analysis [13], to extract the multimodal dispersion curves [14] as well as to expedite  
28 the acquisition process in ultrasonic propagation imaging [15]. In this work, a CS-based approach aimed  
29 at minimizing the SLDV full wavefield acquisition phase is presented.

30 Besides the different application domains, CS methodologies can be distinguished on the basis of two  
31 distinctive features: (i) the selected dictionary of basis functions which produces the sparse representation  
32 of the considered signal, and (ii) the measurement mechanism, which substitutes the traditional Nyquist-  
33 based data collection techniques.

34 A variety of dictionaries have been developed for representing multidimensional signals [16]. These  
35 dictionaries can be either based on an analytic formulation (i.e. *Analytical Dictionaries* such as Fourier,  
36 Wavelets, Gabor atoms), or defined on the basis of a set of realizations of the data (*Learned Dictionaries*).  
37 In this work, Analytical Dictionaries have been used. In fact, the characteristic of guided wave propagation  
38 are strongly dependent on the material and geometrical properties of the inspected medium, and this would  
39 require a specific and time-consuming dictionary learning procedure applied each time the material or  
40 simply the thickness or temperature of the inspected material change. Analytical dictionaries may be less

41 effective than Learned Dictionaries for a given experimental setup, but can be fruitfully employed in  
 42 many applicative contexts without any repeated training. Beside of that, analytical formulations allow for  
 43 fast implicit decompositions, and consequently less computationally-intensive signal recovery procedures.

44 In our approach, the number of scan points acquired in a standard laser vibrometer acquisition is  
 45 decremented by using two different subsampling techniques: the first one is the so called jittered sampling  
 46 which as been already used in seismic applications [11]; the second one is the Farthest point sampling  
 47 [17] which is based on an iterative strategy.

48 The implemented procedure takes into account both suitable sparsity-promoting domains and sample-  
 49 points distribution strategies, achieving the best recovering result possible starting from highly incomplete  
 50 wavefield data. In order to prove its effectiveness, the approach has been validated on signals from  
 51 experimental setups with different kinds of structural defects.

52 The paper is organized as follows: Section II deals with the definition of CS theoretical framework.  
 53 Two approaches for sampling-points distribution are described in Section III, whereas a review of sparsity  
 54 promoting decomposition bases suited for guided wave inspections is provided in Section IV. In Section  
 55 V, experimental results concerning the reconstruction of the sub-sampled wavefield are shown. Finally,  
 56 conclusions and further developments are summarized in Section VI.

## 57 II. COMPRESSIVE SENSING OF WAVEFIELD DATA

58 Compressive Sensing [18] is a theoretical framework which relies on two principles, namely *sparsity*  
 59 and *incoherence*. The first one expresses the idea that a signal's information content can be represented  
 60 into a small amount of data when expressed in terms of a proper basis. While incoherence is related to  
 61 the idea that the elements of the sparsifying basis are poorly correlated with the sampling functions.

62 Let  $\Sigma(x, y, t)$  be the wavefield signal in the spatial and temporal domain,  $s \in \mathbb{R}^n$  is its sampled version,  
 63 acquired according the Nyquist sampling theory. We are interested to recover  $s$  from a small set of linear  
 64 measurements

$$y_i = \langle \Sigma(x, y, t), \varphi_i(x, y) \rangle, \quad i = 1, \dots, m, \quad (1)$$

65 being  $\varphi_i$  the sampling functions. In under-sampled situations the number of available measurements  $m$   
 66 is much smaller than the dimension of the signal  $n$ , and the recovery problem is in general ill-posed and  
 67 admits infinite solutions. Such limitation can be overcome if some further assumptions can be posed.

68 Let us consider a vector  $\alpha \in \mathbb{R}^n$  such that  $s = \Psi\alpha$ , with  $\Psi \in \mathbb{R}^{n \times n}$ . We define the representation  
 69 produced by the basis  $\Psi$  as  $K$ -sparse if  $K$  is the number of nonzero elements of  $\alpha$ . Furthermore,

70 consider a sampling matrix  $\Phi \in \mathbb{R}^{m \times n}$  obtained organizing columnwise the sampling functions  $\varphi_i$ . We  
 71 define *coherence* the measure of the largest correlation between any two elements of the basis  $\Psi$  and  $\Phi$ :

$$\mu(\Phi, \Psi) = \sqrt{n} \cdot \max_{1 \leq i, j \leq n} |\langle \varphi_i, \psi_j \rangle|, \quad (2)$$

72 with  $\mu \in [1, \sqrt{n}]$ . The CS asserts that if the signal has a  $K$ -sparse representation in a basis  $\Psi$  with  
 73  $K \ll n$ , and if the sensing matrix  $\Phi$  is sufficiently uncorrelated with  $\Psi$ , i.e.  $\mu \sim 1$ , then the signal  $s$   
 74 can be recovered by solving a  $\ell_1$  norm minimization problem. More specifically, in [19], it was proven  
 75 that the number of measurements required for the exact recovery depends on the sparsity parameter  $K$ ,  
 76 and quadratically on  $\mu$ :

$$m \geq C \cdot \mu^2(\Phi, \Psi) \cdot K \log(n) \quad (3)$$

77 In practical applications, measurements are affected by noise:

$$y = \Phi \Psi \alpha + z, \quad (4)$$

78 where  $z$  is the noise term. Moreover, real world data are not exactly sparse. Despite this fact, when the  
 79 coefficients of vector  $\alpha$  decay exponentially in absolute value, the signal is still compressible, and the  
 80 approximation of  $\alpha$  which retains its  $K$  largest entries can be recovered [6] by solving the following  
 81 sparsity-promoting problem:

$$\min \|\tilde{\alpha}\|_{\ell_1} \quad \text{subject to} \quad \|\Phi \Psi \tilde{\alpha} - y\|_{\ell_2} \leq \epsilon, \quad (5)$$

82 where  $\epsilon$  bounds the amount of noise in the data.

### 83 III. SAMPLING-POINTS DISTRIBUTION PATTERNS

84 As detailed in the previous section, the design of an efficient compressive sensing protocol requires  
 85 to define a suitable sampling scheme ( $\Phi$ ) and the sparsity-promoting dictionary  $\Psi$  in order to satisfy  
 86 the incoherence condition(2). In this work, the waveform measurement is the one produced by scanning  
 87 devices such as SLDVs in the spatial and temporal domain, and  $n$  is the number of samples which  
 88 should be acquired to respect the Shannon sampling theory (i.e.the *full-resolution* sampling grid). By  
 89 assuming that the SLDV measurements are almost ideally point-like, the sub-sampling matrix  $\Phi$  is given  
 90 by the Dirac (identity) basis in which are removed the rows corresponding to  $n - m$  locations. In this  
 91 section, different strategies to select the preserved  $m$  samples are presented and discussed. It should be  
 92 anticipated that the subsampling is performed just in the spatial domain, since no advantage in terms of  
 93 reconstruction accuracy or reduction of measurement time is achieved by subsampling the wavefield also  
 94 in the time domain.

95 The CS recovery is affected by strong coherent aliases when a simple regular subsampling is performed.  
 96 Such aliases can be avoided with random sub-sampling schemes [20]. Starting from a uniform full-  
 97 resolution grid on a 2D spatial domain, a possible under-sampling scheme can be easily achieved taking  
 98 a random subset of measurements on the grid. Unfortunately, such a scheme can affect the quality of the  
 99 recovery procedure. In fact, there may be excessively large gaps between scan-points causing the fault of  
 100 the reconstruction in these areas. Alternatively, the so called Jittered sampling (JS) can be adopted [21].

101 The jittered subsampling implemented in this work is a bidimensional extension of the one presented  
 102 in [11] and it is based on the following steps: i) regularly decimate the full-resolution grid, and ii)  
 103 subsequently perturb the coarse-grid sample points on the fine grid. More specifically, a discrete uniform  
 104 distribution for the perturbation around the coarse-grid points is considered, so that each location is  
 105 equally likely to be sampled. Further details are provided in Appendix A.

106 A possible alternative is in the Farthest Point sampling (FPS) method [17], which starts from an  
 107 initial small set of random placed samples, and adds iteratively sampling points on the inspected region,  
 108 selecting the next sample to be the farthest point from all previously selected ones, until a certain stopping  
 109 condition is reached (e.g. the desired number of sampling points). The Jittered and FPS sampling schemes  
 110 are illustrated in Fig.1

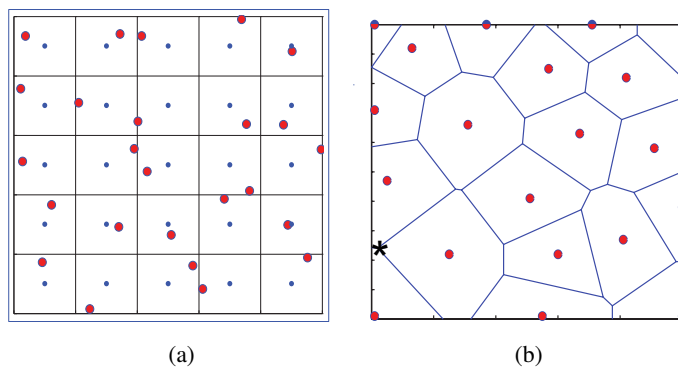


Fig. 1: (a) Jittered subsampling scheme, the dots represent the scanpoints obtained by regularly subsampling the full resolution grid, their position is then randomly perturbed (bigger circles) to define the scanpoint to be acquired in the CS procedure; (b) Farthest Point sampling, the circles represent the initial set of sampling points; such set is enlarged by selecting iteratively the farthest (marked by an asterisk) among the vertices of the Voronoi diagram (solid lines).

111 For each step of the FPS procedure, the farthest point is found by computing the Voronoi diagram  
 112 [22] from the previous samples, and then selecting the farthest among the Voronoi diagram vertices as

113 additional sampling point. When the Voronoi diagrams are computed on the basis of the pure Euclidean  
 114 distance, the FPS method progressively limits the maximum gap between sampling points, thus producing  
 115 a rather uniform sampling distribution. When needed, the sample density can be also adaptively varied  
 116 by following the strategy presented in [17].

#### 117 IV. SPARSITY-PROMOTING DICTIONARIES FOR WAVEFIELD IMAGES

118 Let us focus now the discussion on the matrix  $\Psi$ . Such matrix transforms the signal from the sparse  
 119 representation domain to the domain in which the measurements are acquired (i.e. the spatial and temporal  
 120 domain, as specified in the previous section). In this work, we will evaluate as sparse representation  
 121 domains the ones spanned by the Fourier exponentials, Curvelets, or Wave Atoms. This means that  $\Psi$   
 122 will be the matrix operator which computes the Fourier, Curvelet or Wave Atom inverse transforms,  
 123 respectively.

##### 124 A. Fourier domain

125 The dispersive and multi-modal characteristics of guided wave propagation have been extensively  
 126 studied. A guided wave which travels a distance  $|x - x_{s1}|$  from an ideal actuator (point-like source) can  
 127 be modelled in the frequency domain as a dispersive system whose response is:

$$S_0(f, x) = S_0(f, x_{s1}) \cdot \sum_{i=1}^M A_M(f) e^{-j|x-x_{s1}|k_M(f)} \quad (6)$$

128 being  $S_0(f, x_{s1})$  the Fourier Transform of the excitation pulse at the actuation position  $x_{s1}$ ,  $k_M(f)$   
 129 the frequency-wavenumber dispersion curve for mode  $M$  and  $A_M(f)$  its dispersive attenuation in the  
 130 range of frequencies considered. It follows that in the Fourier domain, the full wavefield components are  
 131 concentrated on the dispersion curves  $k_M(f)$  of the propagating wavemodes. The sparsifying effect of  
 132 the Fourier decomposition can be observed in Fig. 2.

133 Space-time traces related to the simulation of Lamb wave propagation in a 1mm-thick aluminum  
 134 plate, considering a 3-cycle sine wave centered at 30 kHz as excitation pulse, are depicted in Fig. 2(a).  
 135 More specifically, the Semi-analytical Finite Element (SAFE) formulation developed in [23] has been  
 136 used to compute the time waveforms at different distances, considering the following nominal properties  
 137 for aluminum: Young modulus  $E = 69$  GPa, Poisson's coefficient  $\nu = 0.33$  and density  $\rho = 2700$   
 138  $\text{kg/m}^3$ . The frequency/wavenumber representation of the same signal is depicted in Fig. 2(b). It is worth  
 139 noticing that the Fourier representation of the simulated wavefield is much sparser than the time-space

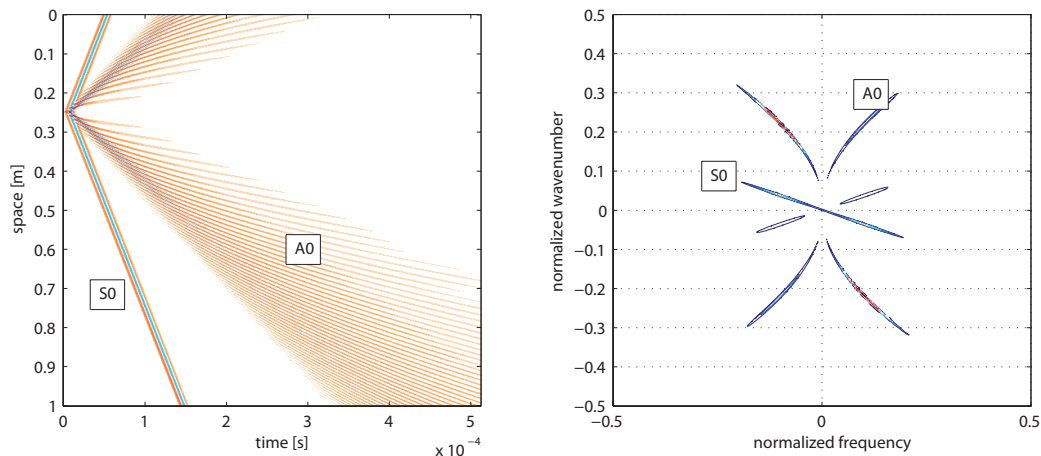


Fig. 2: Simulated propagation of Lamb waves in an aluminum plate. An acoustic source is placed at  $x = 0.25$ . Two wave modes ( $A_0$  and  $S_0$ ) are excited. Because of dispersion, the number of non-negligible samples is quite high in the space-time domain. In the Fourier domain, the signal is confined on the  $k(\omega)$  curves, and the representation is consequently much more sparse.

140 representation, since the information is compressed in few non-negligible Fourier coefficients along the  
 141 dispersion curves of two wave modes ( $A_0$  and  $S_0$ ).

142 The sparsifying properties of the Fourier transform can be shown also by looking at Fig. 3. In this  
 143 figure, such operator is applied to the spatial wavefield captured on a given instant in a simulated setup  
 144 similar to the previous one (although just the  $A_0$  wave is captured in the considered snapshot). It is worth  
 145 noticing how the transform produces a very sparse representation in the wavenumber domain.

146 The representation offered by the Fourier transform has been fruitfully used ([24]) to separate the  
 147 waves scattered by defects from the incident ones. Fourier bases are consequently good candidates for  
 148 the construction of the sparsifying dictionary in the CS recovery procedure. It is also worth noticing that  
 149 the inverse Fourier transforms operator is maximally incoherent with the sampling matrix, because  $\mu$   
 150 attains its minimum at  $\mu = 1$  for the Fourier-Dirac pair.

### 151 *B. Curvelets domain*

152 The curvelet transform (CT) [25] provides a compact architecture for sparse representation of images  
 153 with singularities along curves. For a given 2D function, the transform performs a decomposition in a  
 154 frame of “needle-shaped” waveforms (named curvelets) that are localized not only in position (the spatial

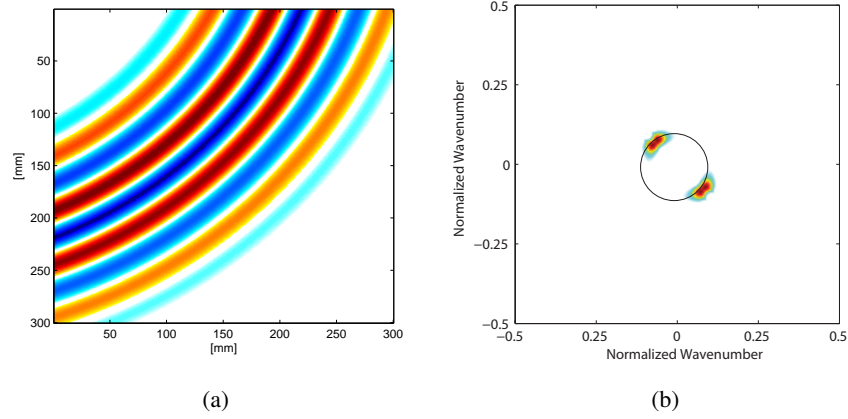


Fig. 3: Simulated propagation of Lamb waves in an aluminum plate. A snapshot of the wavefield related to a  $300 \times 300 \text{mm}^2$  area is depicted. (a). The Fourier transform produces a very sparse representation in the wavenumber domain. (b)

domain) and scale (the wavenumber domain), but also in orientation. The curvelets construction is based on a tiling of the wavenumber domain performed by a couple of strictly bandpass classes of functions.

Let  $\xi = (\xi_1, \xi_2)$  be the wavenumbers along 2D spatial axes. Curvelet functions are indexed by three parameters: a scale  $\nu$ , a direction  $l$  and a position index  $x = (x_1, x_2)$  which specifies the translation  $b_x^{\nu,l}$  of the curvelet waveform. The product of concentric square functions  $\tilde{W}_\nu(\xi)$  and sheared angle functions  $V_\nu(\xi)$  defines Cartesian windows in the wavenumber domain:

$$\tilde{U}_{\nu,l}(\xi) = \tilde{W}_\nu(\xi)V_\nu(S_{\theta_l}, \xi), \quad (7)$$

where  $S_{\theta_l}$  is the shear matrix

$$S_{\theta_l} = \begin{pmatrix} 1 & 0 \\ -\tan \theta_l & 1 \end{pmatrix}, \quad (8)$$

and angles  $\theta_l$  are chosen to define a set of equispaced slopes  $\tan \theta_l = l \cdot 2^{\lfloor \nu/2 \rfloor}$ , with  $l = -2^{\lfloor \nu/2 \rfloor}, \dots, 2^{\lfloor \nu/2 \rfloor} - 1$ . The set of windowing functions  $\tilde{W}_\nu$  provides a decomposition of the wavenumber plane in Cartesian coronae, each divided by sheared functions  $V_\nu$  of  $N_\nu = 4 \cdot 2^{\lfloor \nu/2 \rfloor}$  trapezoids. According to Fig. 4a, the number of shears doubles in each second square. On the other hand, in the space domain the wavenumber localization of  $\tilde{U}_{\nu,l}$  implies the rapid decay away from a  $2^{-\nu}$  by  $2^{-\nu/2}$  rectangle with major axis orthogonal to the direction  $\theta_l$  (see Fig. 5a), so that the support's length and width obey the *parabolic scaling* relation

$$\text{length} \approx 2^{-\nu/2}, \quad \text{width} \approx 2^{-\nu} \quad \Rightarrow \quad \text{width} \approx \text{length}^2, \quad (9)$$

168 An example of curvelet atom for  $\nu =$ ,  $l =$  and  $x =$  is provided in Fig. 5a.

169 In three dimensions (2 spatial and 1 temporal dimensions), the theory is essentially the same, except  
 170 that curvelets are now 3D basis functions of side-length  $2^{-\nu/2}$  in two directions and thickness  $2^{-\nu}$  in the  
 171 orthonormal direction, so that the parabolic scaling relation still holds, and  $\xi = (\xi_1, \xi_2, \xi_3)$  is now related  
 172 to wavenumbers and frequency. 3D curvelets provide valuable sparse representations of 3D objects with  
 173 singularities along smooth surfaces.

174 For a given (either 3- or 2D) signal  $s$  whose Fourier transform is  $S(\xi)$ , the curvelet coefficients can  
 175 be computed as

$$c(\nu, l, x) = \int S(\xi) \tilde{U}_{\nu, l}(\xi) e^{i\langle b_{x, l}^{\nu}, \xi \rangle} d\xi. \quad (10)$$

176 Therefore a practical implementation performs three steps: 1) data are transformed into the frequency  
 177 domain by forward fast Fourier transform (FFT), 2) transformed data are multiplied by the set of window  
 178 functions  $\tilde{U}_{\nu, l}$  and 3) curvelet coefficients are obtained from windowed data by inverse FFT. The com-  
 179 putational complexity is  $O(N^2 \log_2 N)$ . Further details about discrete curvelet transform implementation  
 180 can be found in [25] and [26], while the code (Curvelab package) which computes the curvelet transform  
 181 employed in this study is available at [27].

182 It has been proved that the curvelet operator is the one that produces the sparsest representation of  
 183 wave propagation phenomena [28], and such property potentially allows to reduce the number of sample  
 184 locations, following (3). However, Curvelets and discrete Dirac delta are less incoherent with respect to  
 185 the Fourier-Dirac pair, and this may adversely affect the recovery (see [29]).

### 186 C. Wave Atoms domain

187 Wave atoms [30] represent another tool for multiscale analysis, allowing to expand a multidimensional  
 188 function in a linear combination of localized, directional waveforms. Similarly to curvelets, wave atoms  
 189 provide a tiling of the frequency/wavenumber plane (see Fig. 4(b)) which has been proven to sparsely  
 190 represent oscillatory patterns [30].

191 In the space domain, wave atoms are smoothed oscillating functions whose support is approximately  
 192 a square of size  $2^{-\nu}$  by  $2^{-\nu}$  at scale  $\nu$ , with oscillation of wavelength  $\sim 2^{-2\nu}$  transverse to the ridge,  
 193 while in frequency domain each tile is a  $2^\nu$  by  $2^\nu$  square, at a distance  $\sim 2^{2\nu}$  from the origin, as showed  
 194 in Fig. 4(b).

195 Note that the subscript  $\nu$  indexes the different ‘‘dyadic coronae’’, whereas direction and position are  
 196 indexed by  $l$  and  $x$ , respectively. Fig. 5(b) exhibits a wave atom for  $\nu =$ ,  $l =$  and  $x =$ , which shows a  
 197 more isotropic aspect ratio w.r.t. curvelet in Fig. 5(a).

198 All the transformations considered in this section (including curvelets and wave atoms) make a central  
 199 use of discrete Fourier transform algorithms such as the Fast Fourier Transform (FFT). Due to its implicit  
 200 periodicity, FFT may cause reconstruction artifacts across boundaries. A way of avoiding this unwanted  
 201 outcome is to work on the discrete cosine transform of the original domain, in place of the Fourier  
 202 transform, with no penalty on redundancy or computational complexity. The complete mathematical  
 203 treatment can be found in [31], while the code used in this study is available at [32].

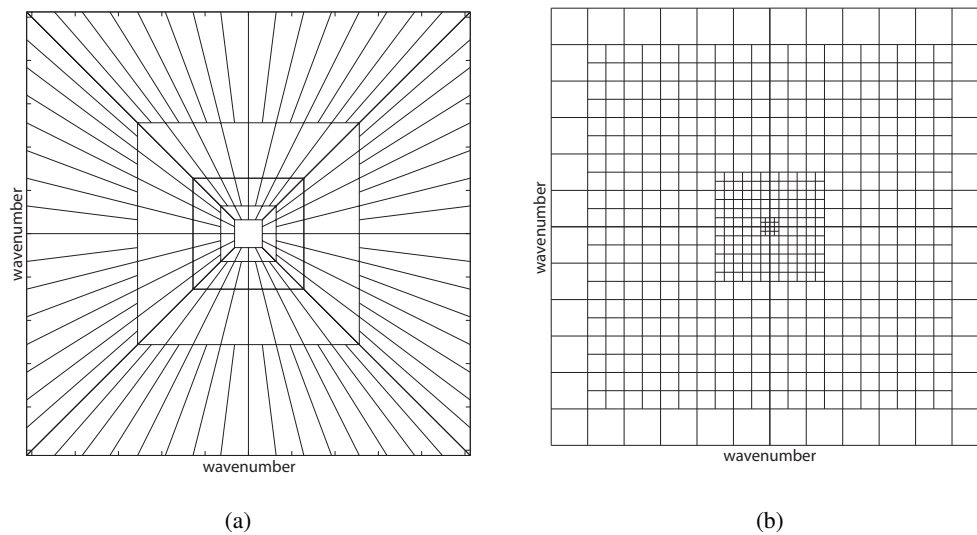


Fig. 4: (a) Curvelet dyadic decomposition of the wavenumber plane; (b) wave atom tiling of the wave number plane.

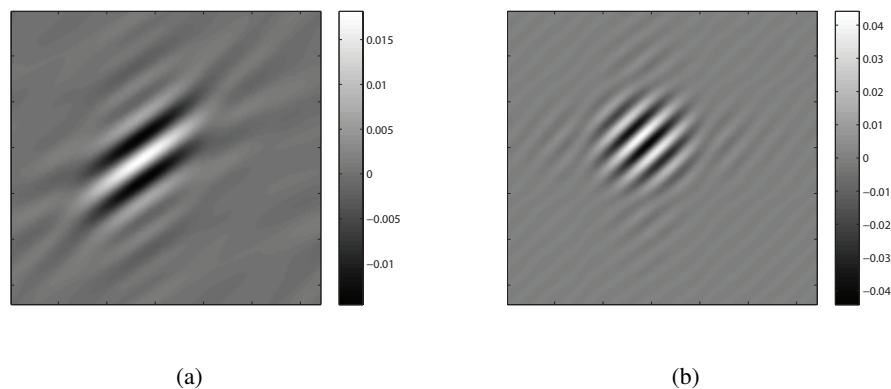


Fig. 5: Examples of basis functions: (a) curvelet atom; (b) wave atom

## V. EXPERIMENTAL RESULTS AND DISCUSSION

The results of the CS reconstruction of a wavefield signal acquired on two distinct setups were evaluated in order to assess the proposed approach. The first setup is constituted by a 1.5 mm thick 6061 aluminum plate (638 mm  $\times$  558 mm wide). The presence of a defect was emulated by a 12 mm diameter cylindrical mass bonded on the surface of the plate. A 10 mm diameter PZT transducer was used to excite the guided field in the structure, while the plate response was recorded through a Polytec PSV400M2 SLDV over a rectangular area of 150 mm  $\times$  155 mm, in a grid of 141  $\times$  151 equispaced points.

The second setup is constituted by a glass fibre reinforced polymer (GFRP) plate (4 unidirectional glass fibre layers oriented along x axis, thickness equal to 3.2 mm). Three 0.5 mm wide and 70% of the specimen thickness deep notch cuts were machined by a sharp tool. The excitation signal was generated by an arbitrary waveform generator, amplified to 400Vpp by a dedicated PZT amplifier. The excitation signal was applied to a round piezoelectric transducer (10 mm diameter). Out of plane displacements were registered by a SLDV on dense grid of (385  $\times$  389) equally spaced points.

The CS procedure was implemented in Matlab using the SPGL1 toolbox [33] which iteratively solves the sparsity-promoting problem in Eq. (5), with the support of the suite Sparco [34]. The outcomes of the procedure were compared in terms of both computational time and Signal to Noise Ratio (SNR), defined as

$$20 \cdot \log_{10} \left( \frac{\|u(x_1, x_2, t)\|}{\|u_r(x_1, x_2, t) - u(x_1, x_2, t)\|} \right), \quad (11)$$

where  $u$  is the signal acquired on the dense grid, and  $u_r$  is the recovered wavefield signal, by varying the number of iterations of the SPGL1 algorithm (detailed in Appendix B), and the sparsifying basis.

To qualitatively judge the performance of the presented approach, the recovery of two snapshots related to the different setups are illustrated in Fig. 6 and 7. In Fig. 6(a), the signal acquired on the aluminum plate at a given time instant is shown along with the ones recovered with different dictionaries (Fig. 6(c)-(f)). The recovery was performed starting from less than 34% measurements with respect to the original grid (the JS mask is illustrated in Fig. 6(b) with black square dots). It is worth noticing the substantial agreement of all the recovered signals to the acquired one, which proves the effectiveness of the procedure. Furthermore, the presented results are much more accurate than the ones achieved by simply interpolating the sub-sampled signal, as can be seen by looking at the linear interpolation results depicted in Fig. 6(c). Similarly, the recovery of the wavefield acquired on the composite panel is very effective, as can be seen in Fig. 7.

In Fig. 8, the results of the implemented procedure applied to the first setup are depicted in terms of

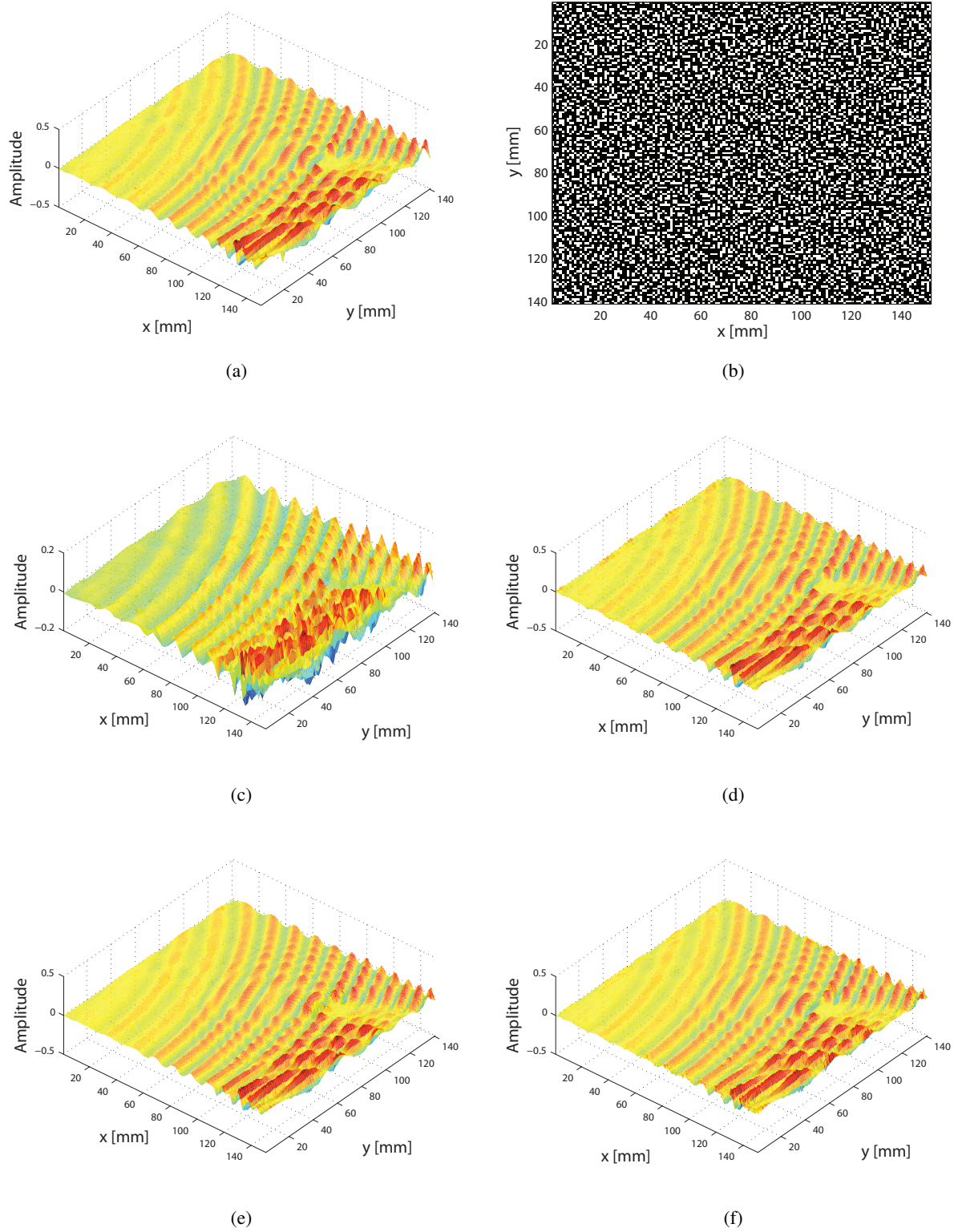


Fig. 6: (a) Original full wavefield on aluminum plate at a given time instant, (b) JS mask used to undersample the acquisitions, (c) linear interpolation, (d) Full wavefield recovered with FFT 3D, (e) Wave Atom, (f) 2D Curvelet domain by less than 34% measurements respect to the original sampling grid.

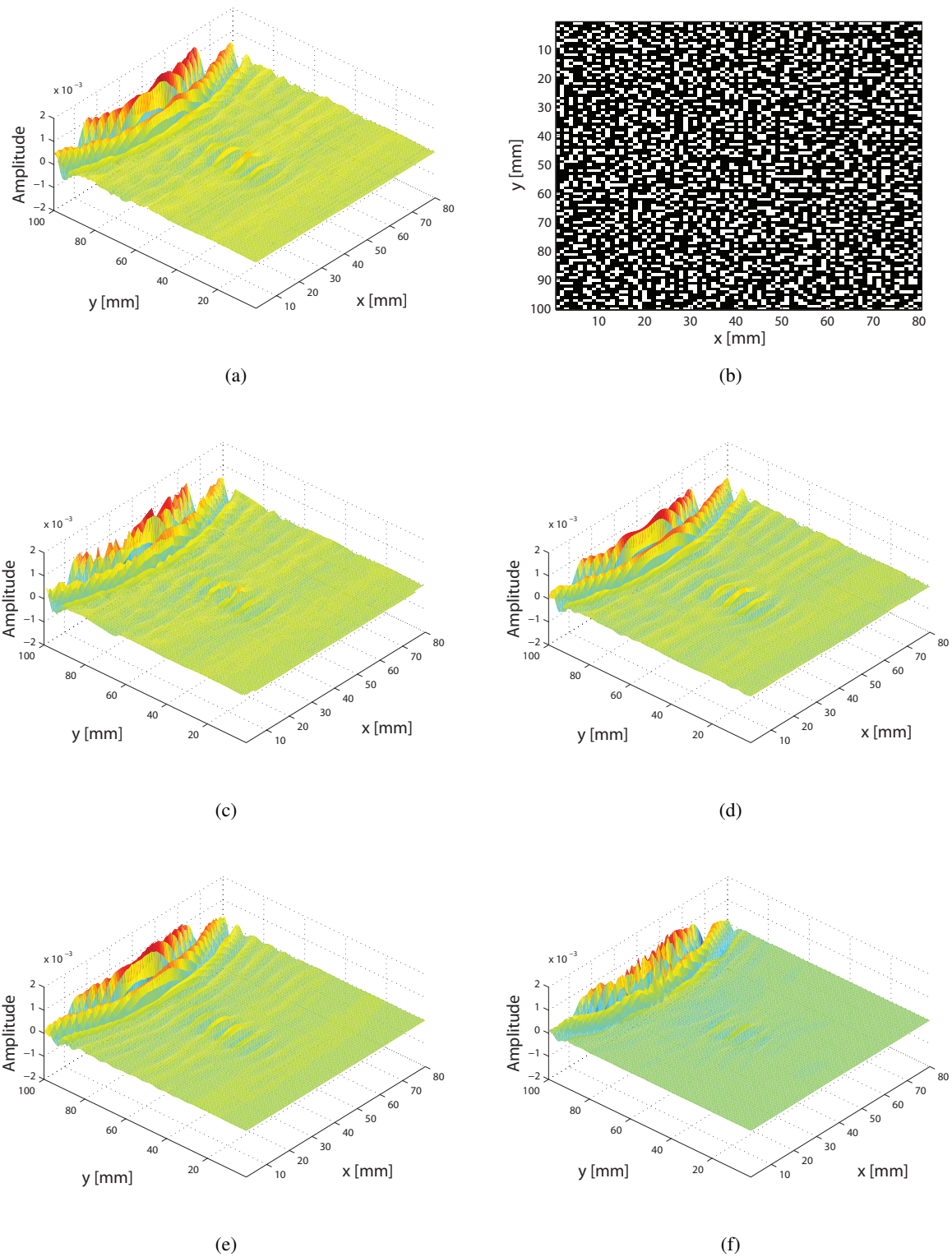


Fig. 7: (a) Original full wavefield on composite plate at a given time instant, (b) JS mask used to undersample the acquisitions, (c) linear interpolation, (d) Full wavefield recovered with FFT 3D, (e) Wave Atom, (f) 2D Curvelet domain by less than 34% measurements respect to the original sampling

234 the number of iteration a priori set for the recovery algorithm SPGL1. By looking at Fig. 8 (a), it can  
235 be noticed that the quality of the reconstruction reach its maximum value after about 90 iterations in all  
236 the considered cases. In particular, the best performance in terms of SNR is achieved by adopting the  
237 Wave atom or the 3D Fourier transform as sparsifying operators.

238 It is important to point out that our main aim it to evaluate the capability to preserve the informative  
239 content of the signal (i.e. high SNRs) while reducing the number of acquisition points, because such  
240 reduction implies a parallel reduction of the acquisition time and consequently a more efficient usage  
241 of the scanning equipment. In fact, in the proposed approach the computational resources necessary to  
242 perform the reconstruction can be used off-line, while the acquisition process can run independently.  
243 Despite this, it also is interesting to evaluate the computational time which is necessary to perform  
244 the full-resolution signal recovery. In this sense, the best trade-off between SNR and computational  
245 time is the one offered by the 3D Fourier (3D FT) basis which provides high SNRs even with few  
246 iterations and a very fast processing. In such a case, the solver converges in about 30 iterations in few  
247 minutes of computational time with an Intel i5™ Processor. Conversely, for Curvelet (2D CT) and  
248 Wave Atom 2D domains (WA), the results are mainly similar in terms of SNR, but they require several  
249 hours of computational times. The 3D Curvelet basis (3D CT) recovery has relatively poor performances,  
250 this result is somehow in contrast with the effective and sparse representation of wavefield recordings  
251 produced by the Curvelet transform ([35]). One possible explanation is in the relatively small support  
252 of curvelet atoms which may produce artefacts in case of sparse subsampling, because of the relatively  
253 high coherence among sparsifying dictionary and measurement functions.

254 The recovery algorithm achieves high values of SNR with a reduced number of SPGL1 iterations  
255 when high percentages of scanpoints are retained. The results in term of recovery time using a jittered  
256 undersampled grid for the cases of 33% and 90% retained scanpoints are shown in Table I. The number  
257 of iteration for the SPGL1 recovery algorithm has been set to 30 and 15 in order to achieve an SNR  
258 equal to 30dB in both cases.

259 As can be observed in Table I, the number of SPGL1 iterations is not directly proportional to the com-  
260 putational time, so that the percentage of retained scanpoints just partially influences the computational  
261 cost of the reconstruction procedure.

262 In Table II the results of the reconstruction of the second setup wavefield signal in the 3D Fourier basis  
263 with 30 iterations by means of Random, Jittered and FPS distributions are shown. For each sampling  
264 strategy, 20 realizations were considered. The minimum and maximum values of the achieved SNRs are  
265 reported, retaining the 15% and 33% of the original grid scanpoints. Even though the Farthest Point

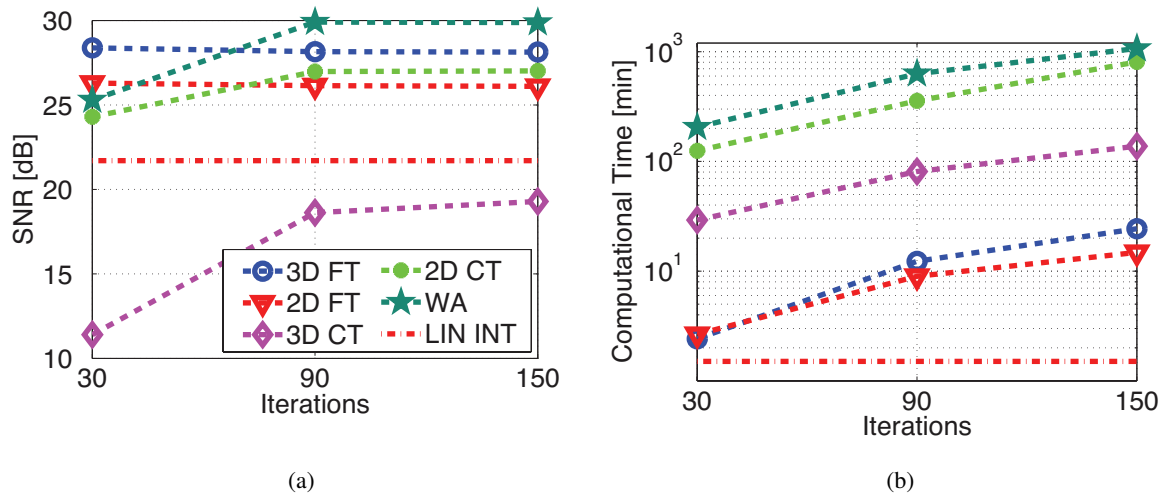


Fig. 8: (a) SNR performances achieved, and (b) computational time needed to recover the full wavefield with different sparsifying basis as a function of the number of iterations of the SPGL1 algorithm. The dot-dashed lines indicate the performances achieved by the simple linear interpolation.

TABLE I: Computational Time of the CS recovery obtained from: a) full wavefield signal random subsampled in 33% locations respect to the original grid distributed with 2D Jittered approach (30 iteration for the SPGL1 algorithm); b) considering 90% of the grid points (15 iteration for the SPGL1 algorithm).

| Dictionary | Computational Time (a) [min] | Computational Time (b) [min] |
|------------|------------------------------|------------------------------|
| 3D FFT     | 12.31                        | 9.03                         |
| 2D FFT     | 8.99                         | 6.57                         |
| 3D CT      | 81.00                        | 71.27                        |

266 strategy produces a more uniform distribution, JS yields a better recovery in terms of SNR. This is in  
 267 line with the results reported in [36], for seismic data acquisitions. The performance achieved with the  
 268 FPS strategy is inferior even w.r.t the pure random selection of scan-points. However, this is true for  
 269 a global metric such as the SNR but not for the maximum of the local error (i.e.  $\|u_r - u\|_\infty$ ). It was  
 270 verified that on the same dataset the maximum local error produced by the random distribution is 7%  
 271 higher w.r.t. the FPS, and 13.% higher w.r.t. the JS, on average.

272 A possible benefit of the FPS strategy is the capability for progressive sampling, which allows to vary  
 273 dynamically the resolution during the acquisition process. Such capability can be extremely useful when  
 274 high sample density is needed in areas with fine details: FPS samples distribution can be altered defining

TABLE II: Reconstruction SNRs in the Fourier domain after 30 iterations of the CS problem solver for different sampling-point distribution strategies (15% or 33% samples preserved, 20 grids generated for each strategy).

| Sampling scheme | SNR [dB] (15%) |              | SNR [dB] (33%) |              |
|-----------------|----------------|--------------|----------------|--------------|
|                 | min            | max          | min            | max          |
| Random          | 15.94          | 17.37        | 27.72          | 29.46        |
| Jittered        | <b>16.63</b>   | <b>17.55</b> | <b>29.43</b>   | <b>30.74</b> |
| FPS             | 14.46          | 15.49        | 24.83          | 26.23        |

275 an alternative weighted-metric over the spatial domain, therefore providing a valuable adaptive sampling  
 276 scheme (see Sec. III, and [17]).

## 277 VI. CONCLUSIONS

278 In this paper, a CS framework for acoustic wavefield acquisitions was presented. The proposed frame-  
 279 work aims at minimizing the number of scan-point locations over the surface of the inspected structure.  
 280 Both sampling-point distribution strategies and sparsity-promoting dictionaries were investigated in order  
 281 to produce the best recovery for a sub-sampled wavefield signal obtained with a scanning laser Doppler  
 282 vibrometer.

283 The decomposition of the signal in the Fourier domain turned out to be the more effective solution,  
 284 leading to a very fast and accurate recovery starting from less than 34% of measurements with respect  
 285 to the original sampling grid. This result can be ascribed (i) to the fast algorithms which compute the  
 286 Fourier transform, (ii) to the sparse representation of Lamb wave signals offered by the Fourier domain,  
 287 as well as (iii) to the high incoherence of Fourier exponentials with the examined sampling schemes, and  
 288 demonstrates the great potential of the CS approach.

289 Among the future developments, an adaptive sampling-point distribution strategy could be developed  
 290 taking advantage of the progressiveness of the FPS scheme. It is possible indeed to introduce case-specific  
 291 metrics in order to place each new sampling-point in the position that minimize the local recovery error,  
 292 further improving the tradeoff between the number of scan-points and accuracy in the reconstructions.

## APPENDIX A: JITTERED SUBSAMPLING SCHEME

Let us assume that the full resolution grid is a cartesian grid of scanpoints in which each vertex has  
 coordinates  $(i * \Delta, j * \Delta)$ , with  $i \in [0, 1, \dots, I]$ ,  $j \in [0, 1, \dots, J]$  and  $\Delta$  being the spatial spacing (set

according to the Nyquist sampling theorem). If  $\gamma$  is the downsampling factor, the coordinates of the Jittered subsampled grid are given by:

$$\begin{aligned} x_1 &= i_s \cdot \frac{\Delta}{\sqrt{\gamma}} + \epsilon_i, i_s \in [0, 1, \dots, I \cdot \sqrt{\gamma}] \\ x_2 &= j_s \cdot \frac{\Delta}{\sqrt{\gamma}} + \epsilon_j, j_s \in [0, 1, \dots, J \cdot \sqrt{\gamma}] \end{aligned}$$

where the random variables  $\epsilon_i$  and  $\epsilon_j$  are independently and identically distributed (i.i.d.) according to a uniform distribution on the interval  $[-\Delta/\sqrt{\gamma}, \Delta/\sqrt{\gamma}]$ .

#### APPENDIX B: SPGL1 ALGORITHM

The Spectral Projected Gradient for  $\ell_1$  minimization (SPGL1) algorithm computes the solution of **5** by solving the sequence of the following subproblems:

$$\alpha^{\tau_i} = \arg \min_{\tilde{\alpha} \in R^n} \|\Phi\Psi\tilde{\alpha} - y\|_{\ell_2} \quad \text{subject to} \quad \|\tilde{\alpha}\|_{\ell_1} \leq \tau_i$$

The algorithm starts by defining the first tentative solution  $\alpha^0$  and the initial value for the parameter  $\tau_0 = \|\alpha^0\|_{\ell_1}$ . Then the updating of  $\tau$  is performed by traversing the Pareto curve described by the function  $\eta(\tau) = \|\Phi\Psi\alpha^{\tau_i} - y\|_{\ell_2}$ :

$$\tau_{i+1} = \tau_i + \frac{\eta(\tau_i) - \epsilon}{\eta'(\tau_i)}$$

The iterations are stopped when  $\|\Phi\Psi\alpha^{\tau_i} - y\|_{\ell_2} = \epsilon$  or some alternative stopping conditions (e.g. the maximum number of iterations) are met.

#### ACKNOWLEDGEMENTS

The authors gratefully acknowledge Prof. Ruzzene (Georgia Institute of Technology), and Prof. Ostachowicz (Polish Academy of Sciences) for the provided SLDV acquisitions. The research leading to these results has been partially supported from the SARISTU project (Grant Agreement no. 284562) and from the Harmonia project (National Science Centre Poland funds, decision number DEC-2012/06/M/ST8/00414).

## REFERENCES

- [1] A. Raghavan and C. E. S. Cesnik, "Review of guided-wave structural health monitoring," *The Shock and Vibration Digest*, vol. 39, no. 2, pp. 91–114, March 2007.
- [2] J. L. Rose, "A baseline and vision of ultrasonic guided wave inspection potential," *Journal of Pressure Vessel Technology*, vol. 124, pp. 273–282, August 2002.
- [3] H. Sohn, D. Dutta, J. Y. Yang, M. D. Simio, S. Olson, and E. Swenson, "Automated detection of delamination and disbond from wavefield images obtained using a scanning laser vibrometer," *Smart Materials and Structures*, vol. 20, March 2011.
- [4] P. Sriram, S. Hanagud, and J. I. Craig, "Scanning laser doppler techniques for vibration testing," *Experimental Techniques*, vol. 16, no. 6, pp. 21–26, November 1992.
- [5] W. Staszewski, B. Lee, L. Mallet, and F. Scarpa, "Structural health monitoring using scanning vibrometry: I. lamb wave sensing," *Smart Materials and Structures*, vol. 13, no. 2, pp. 251–260, February 2004.
- [6] E. Candès and M. Wakin, "An introduction to compressive sampling," *IEEE Signal Processing Magazine*, vol. 25, no. 2, pp. 21–30, March 2008.
- [7] H. Liebgott, R. Prost, and D. Friboulet, "Pre-beamformed RF signal reconstruction in medical ultrasound using compressive sensing," *Ultrasonics*, vol. 53, no. 2, pp. 525–533, 2013.
- [8] M. F. Schiffrer and G. Schmitz, "Fast pulse-echo ultrasound imaging employing compressive sensing," in *Proc. IEEE Int. Ultrasonics Symposium (IUS)*, 2011, pp. 688–691.
- [9] C. Quinsac, A. Basarab, and D. Kouamé, "Frequency domain compressive sampling for ultrasound imaging," *Advances in Acoustics and Vibration*, vol. 2012, 2012.
- [10] N. Wagner, Y. C. Eldar, and Z. Friedman, "Compressed beamforming in ultrasound imaging," *Signal Processing, IEEE Transactions on*, vol. 60, no. 9, pp. 4643–4657, 2012.
- [11] W. Tang, J. Ma, and F. J. Herrmann, "Optimized compressed sensing for curvelet-based seismic data reconstruction," *preprint*, vol. 280, 2009.
- [12] F. J. Herrmann, M. P. Friedlander, and O. Yilmaz, "Fighting the curse of dimensionality: compressive sensing in exploration seismology," *Signal Processing Magazine, IEEE*, vol. 29, no. 3, pp. 88–100, 2012.
- [13] A. Perelli, T. Di Ianni, A. Marzani, L. De Marchi, and G. Masetti, "Model-based compressive sensing for damage localization in lamb wave inspection," *Ultrasonics, Ferroelectrics and Frequency Control, IEEE Transactions on*, vol. 60, no. 10, 2013.
- [14] J. Harley and J. Moura, "Sparse recovery of the multimodal and dispersive characteristics of Lamb waves," *Journal of the Acoustical Society of America*, vol. in press.
- [15] D. Mascarenas, S. Chong, G. Park, J. Lee, and C. Farrar, "Application of compressed sensing to 2-d ultrasonic propagation imaging system data," in *Proc. 6th European Workshop on Structural Health Monitoring*, 2012, pp. 1–8.
- [16] R. Rubinstein, A. M. Bruckstein, and M. Elad, "Dictionaries for sparse representation modeling," *Proceedings of the IEEE*, vol. 98, no. 6, pp. 1045–1057, 2010.
- [17] Y. Eldar, M. Lindenbaum, M. Porat, and Y. Zeevi, "The farthest point strategy for progressive image sampling," *IEEE Transactions on Image Processing*, vol. 6, no. 9, pp. 1305–1315, September 1997.
- [18] E. Candès, J. Romberg, and T. Tao, "Robust uncertainty principles: Exact signal reconstruction from highly incomplete frequency information," *IEEE Transactions on Information Theory*, vol. 52, no. 2, pp. 489–509, February 2006.
- [19] E. Candes and J. Romberg, "Sparsity and incoherence in compressive sampling," *Inverse problems*, vol. 23, no. 3, p. 969, 2007.

- [20] G. Hennefent and F. J. Herrmann, "Simply denoise: wavefield reconstruction via jittered under-sampling," *Geophysics*, vol. 73, no. 3, pp. 19–28, May 2008.
- [21] R. L. Cook, "Stochastic sampling in computer graphics," *ACM Transactions on Graphics*, vol. 5, no. 1, pp. 51–72, January 1986.
- [22] A. Okabe, B. Boots, and K. Sugihara, *Spatial Tessellations - Concepts and Applications of Voronoi Diagrams*. John Wiley & Sons, Chicester, 2000.
- [23] A. Marzani and S. Salamone, "Numerical prediction and experimental verification of temperature effect on plate waves generated and received by piezoceramic sensors," *Mechanical Systems and Signal Processing*, vol. 30, no. 0, pp. 204 – 217, 2012.
- [24] M. Ruzzene, "Frequency-wavenumber domain filtering for improved damage visualization," *Smart Materials and Structures*, vol. 16, pp. 2116–2129, October 2007.
- [25] J. Ma and G. Plonka, "The curvelet transform," *IEEE Signal Processing Magazine*, vol. 27, no. 2, pp. 118–133, March 2010.
- [26] E. Candès, L. Demanet, D. Donoho, and L. Ying, "Fast discrete curvelet transforms," *Applied and Computational Mathematics*, California Institute of Technology, Tech. Rep., 2005.
- [27] [Online]. Available: <http://www.curvelet.org>
- [28] E. J. Candes and L. Demanet, "The curvelet representation of wave propagators is optimally sparse," *Communications on Pure and Applied Mathematics*, vol. 58, no. 11, pp. 1472–1528, 2005.
- [29] F. J. Herrmann and G. Hennenfent, "Non-parametric seismic data recovery with curvelet frames," *Geophysical Journal International*, vol. 173, no. 1, pp. 233–248, 2008.
- [30] L. Demanet, "Curvelets, wave atoms and wave equations," Ph.D. dissertation, California Institute of Technology, 2006.
- [31] L. Demanet and L. Ying, "Curvelets and wave atoms for mirror-extended images," *Proc. SPIE, Wavelets XII*, vol. 6701, no. 67010J, September 2007.
- [32] [Online]. Available: <http://www.waveatom.org>
- [33] E. van den Berg and M. P. Friedlander, "Probing the pareto frontier for basis pursuit solutions," *SIAM J. on Scientific Computing*, vol. 31, no. 2, pp. 890–912, November 2008.
- [34] E. van den Berg, M. P. Friedlander, F. J. Herrmann, R. Saab, and O. Yilmaz, "Sparco: A testing framework for sparse reconstruction," Department of Computer Science, University of British Columbia, Tech. Rep., 2007.
- [35] L. D. Marchi, E. Baravelli, M. Ruzzene, N. Speciale, and G. Masetti, "Guided wave expansion in warped curvelet frames," *IEEE Transactions on Ultrasonics, Ferroelectrics and Frequency Control*, vol. 59, no. 5, pp. 949–957, May 2012.
- [36] R. Shahidi, G. Tang, J. Ma, and F. J. Herrmann, "Application of randomized sampling schemes to curvelet-based sparsity-promoting seismic data recovery," *Geophysical Prospecting*, vol. 61, no. 5, pp. 973–997, September 2013.

**Tommaso Di Ianni** was born in Torremaggiore, Foggia, Italy, in 1988. He received the Master of Science degree in Electronic Engineering in 2014 at the University of Bologna with a thesis on Compressive Sensing based Damage Detection. Actually, he is pursuing the Ph.D.degree at the Technical University of Denmark.

February 10, 2015

DRAFT

**Luca De Marchi** received the Dr.Eng. and Ph.D. Degrees in Electronic Engineering respectively in 2002 and 2006 from the University of Bologna. At the end of 2002, he joined the Department of Electronics, Computer Sciences and Systems (DEI) at the University of Bologna. Currently, he is also with the Advanced Research Center for Electronic Systems (ARCES). His current research interests are in ultrasonic signal analysis for structural health monitoring applications.

**Alessandro Perelli** was born in Senigallia, Ancona, Italy, in 1985. He received the Master of Science degree in Electronic Engineering in October 2010 and his Bachelor of Science in Electronic Engineering in 2007, both at the University Polytechnic of Marche, Ancona (Italy). Since September 2012 he has been a visiting research scholar at the Ultrasound Group of University of Leeds. In 2014 he received the Ph.D. degree in Electronic Engineering at the Department of Electronics, Computer Science and Systems DEI - University of Bologna. Since 2014 is Research Associate at the University of Edinburgh.

**Alessandro Marzani** received the B.S. in civil eng. from the Univ. of Bologna, Italy, in 2001; the M.S. in structural eng. from the Univ. of California, San Diego, USA, in 2004; and the Ph.D. in eng. of materials and structures from the Univ. of Calabria, Cosenza, Italy, in 2005. Since 2014, he is an Associate Prof. of Structural Mechanics at the Department of Civil, Chemical, Environmental and Materials Engineering (DICAM), Univ. of Bologna. His research interests include guided wave-based nondestructive and monitoring techniques of materials and structures, signal processing strategies, and numerical modeling.